molecular pharmaceutics

articles

Peptidic Targeting of Phosphatidylserine for the MRI Detection of Apoptosis in Atherosclerotic Plaques

Carmen Burtea,[†] Sophie Laurent,[†] Eric Lancelot,[‡] Sébastien Ballet,[‡] Oltea Murariu,[†] Olivier Rousseaux,[‡] Marc Port,[‡] Luce Vander Elst,[†] Claire Corot,[‡] and Robert N. Muller*[,†]

Department of General, Organic and Biomedical Chemistry, NMR and Molecular Imaging Laboratory, University of Mons, 19, Avenue Maistriau, Mendeleev Building, B-7000 Mons, Belgium, and Guerbet, Research Center, 16-24 rue Jean Chaptal, 93600 Aulnay-sous-Bois, France

Received November 14, 2008; Revised Manuscript Received July 23, 2009; Accepted September 10, 2009

Abstract: Molecular and cellular imaging of atherosclerosis has garnered more interest at the beginning of the 21st century, with aims to image *in vivo* biological properties of plaque lesions. Apoptosis seems an attractive target for the diagnosis of vulnerable atherosclerotic plaques prone to a thrombotic event. The aim of the present work was to screen for apoptosis peptide binders by phage display with the final purpose to detect apoptotic cells in atherosclerotic plaques by magnetic resonance imaging (MRI). A phosphatidylserine-specific peptide identified by phage display was thus used to design an MRI contrast agent (CA), which was evaluated as a potential *in vivo* reporter of apoptotic cells. A library of linear 6-mer random peptides was screened *in vitro* against immobilized phosphatidylserine. Phage DNA was isolated and sequenced, and the affinity of peptides for phosphatidylserine was evaluated by enzyme-linked immunosorbent assay. The phosphatidylserine-specific peptide and its scrambled homologue were attached to a linker and conjugated to DTPA-isothiocyanate. The products were purified by dialysis and by column chromatography and complexed with gadolinium chloride. After their evaluation using apoptotic cells and a mouse model of liver apoptosis, the phosphatidylserine-targeted CA was used to image atherosclerotic lesions on ApoE$^{-/-}$ transgenic mice. Apoptotic cells were detected on liver and aorta specimens by the immunostaining of phosphatidylserine and of active caspase-3. Sequencing of the phage genome highlighted nine different peptides. Their alignment with amino acid sequences of relevant proteins revealed a frequent homology with Ca^{2+} channels, reminiscent of the function of annexins. Alignment with molecules involved in apoptosis provides a direct correlation between peptide selection and utility. The *in vivo* MRI studies performed at 4.7 T provide proof of concept that apoptosis-related pathologies could be diagnosed by MRI with a low molecular weight paramagnetic agent. The new CA could have real potential in the diagnosis and therapy monitoring of atherosclerotic disease and of other apoptosis-associated pathologies, such as cancer, ischemia, chronic inflammation, autoimmune disorders, transplant rejection, neurodegenerative disorders, and diabetes mellitus. The phage display-derived peptide could also play a potential therapeutic role through anticoagulant activity by mimicking the role of annexin V, the endogenous ligand of phosphatidylserine.

Keywords: Phage display; peptide; apoptosis; atherosclerosis; MRI; molecular imaging

1. Introduction

Among the most incapacitating diseases, acute atherothrombotic syndromes represent the foremost cause of morbidity and mortality worldwide. Despite major advances in the treatment of atherosclerosis, a large number of the disease victims die suddenly although presenting an appar-

* Corresponding author: Professor Robert N. Muller, Department of General, Organic and Biomedical Chemistry, NMR and Molecular Imaging Laboratory, University of Mons, 19, Avenue Maistriau, Mendeleev Building, B-7000 Mons, Belgium. Tel/fax: +32-65373520. E-mail: robert.muller@umons.ac.be.

[†] University of Mons-Hainaut.

[‡] Guerbet, Research Center.

10.1021/mp900106m CCC: $40.75
Published on Web 09/10/2009

ently healthy constitution without symptoms previously. Consequently, world joint efforts were focused on the development of various diagnostic imaging strategies aiming to identify high-risk patients. Magnetic resonance imaging (MRI) could play a major role because it can be reiterated noninvasively and provides high-resolution images of the vessel wall. However, most of the existing imaging approaches assess the structural components of atherosclerotic plaque (e.g., fibrous cap thickness, size of the lipid core).[1]

Molecular and cellular imaging of atherosclerosis has garnered more interest at the beginning of the 21st century, with aims to image *in vivo* biological properties of plaque lesions. The atherosclerosis-targeted contrast agents (CAs) under development for plaque imaging must supply accurate information on biological processes, which should be complementary to the clinical assessments currently available.[2]

Apoptosis, or programmed cell death, is an active, genetically controlled process that removes unwanted or damaged cells. This process is indispensable for normal growth and development, for immunoregulation and homeostasis, but its inhibition or overactivation is associated with disease.[3] The contribution of apoptosis to the instability of atherosclerotic lesion has been well documented.[4,5] Apoptosis of macrophages and of smooth muscle cells (SMC) contributes to the expansion of the necrotic core and thinning of the fibrous cap, and possibly plays a major role in the process of plaque rupture and thrombus formation. Tissue factor activity is greatly influenced by phosphatidylserine (PS), which is exposed on apoptotic macrophages within the lipid core, contributing to the procoagulant activity of the plaque.

Apoptosis seems an attractive target for the diagnosis of vulnerable atherosclerotic plaques prone to a thrombotic event. PS exposure on the outer leaflet of the cell membrane is one of the earliest detectable molecular events in apoptosis. A PS targeted CA could therefore identify vulnerable atherosclerotic plaques and play a potential therapeutic role through anticoagulant activity by mimicking the role of annexin V (AnnV), the endogenous ligand of PS.

Several imaging methods have been employed to detect apoptosis which aim to assist the diagnosis and therapy of apoptosis-related pathologies. Among them, diffusion-weighted MRI and imaging with radiolabeled AnnV are the most popular.[6,7] Other molecules employed in apoptosis imaging were the C_2 domain of synaptotagmin I that binds to anionic phospholipids in cell membranes,[8] a small molecular probe identified by ApoSense technology,[9] or peptide-expressing bacteriophages that were used to detect apoptotic cells in liver[10] or blood.[11] Unfortunately, the application of diffusion-weighted MRI is limited because the method relies on strong magnetic field gradients and is therefore sensitive to motion artifacts. In addition, the magnitude of changes is small, while the distinction between the tissue (e.g., the tumor tissue) shrinkage, necrosis, and other processes that can occur with therapy may be difficult. Therefore, more studies are needed to confirm the validity of diffusion-weighted imaging as a marker of therapeutic efficacy in the clinic.[12,13] Among the drawbacks of protein (i.e., AnnV and synaptotagmin I) implementation in clinical applications, we may cite the cost of production, their antigenicity, and the restrained diffusion to the targeted sites due to their larger size. Peptides provide now valuable alternatives to biopharmaceuticals (i.e., antibodies) that bind protein targets with high affinity and specificity, and many medicines marketed today are from this class of small molecule agents.[14] The ApoSense probe is an amphipathic low molecular weight apoptosis marker, but its cell membrane target is still not known.[13,15] In the case of the other phage display-derived peptides published to date,[10,11] no CA was yet developed or validated in *in vivo* models of apoptosis.

Imaging probes targeted to a certain disease biomarker, such as the apoptotic one, became very popular during the

(1) Sanz, J.; Fayad, Z. A. Imaging of atherosclerotic cardiovascular disease. *Nature* **2008**, *451*, 953–957.

(2) Jaffer, F. A.; Libby, P.; Weissleder, R. Molecular and cellular imaging of atherosclerosis - emerging applications. *J. Am. Coll. Cardiol.* **2006**, *47*, 1328–1338.

(3) Thatte, U.; Dahanukar, S. Apoptosis, clinical relevance and pharmacological manipulation. *Drugs* **1997**, *54*, 511–532.

(4) Tabas, I. Apoptosis and plaque destabilization in atherosclerosis: the role of macrophage apoptosis induced by cholesterol. *Cell Death Differ.* **2004**, *11*, S12–S16.

(5) Tedgui, A.; Mallat, Z. Apoptosis, a major determinant of atherothrombosis. *Arch. Mal. Coeur. Vaiss.* **2003**, *96*, 671–675.

(6) Blankenberg, F. G. Recent advances in the imaging of programmed cell death. *Curr. Pharm. Des.* **2004**, *10*, 1457–1467.

(7) Boersma, H. H.; Kietselaer, B. L. J. H.; Stolk, L. M. L.; Bennaghmouch, A.; Hofstra, L.; Narula, J.; Heidendal, G. A. K.; Reutelingsperger, C. P. M. Past, present, and future of annexin A5: from protein discovery to clinical applications. *J. Nucl. Med.* **2005**, *46*, 2035–2050.

(8) Jung, H.; Kettunen, M. I.; Davletov, B.; Brindle, K. Detection of apoptosis using the C2A domain of synaptotagmin I. *Bioconjugate Chem.* **2004**, *15*, 983–987.

(9) Aloya, R.; Shirvan, A.; Grimberg, H.; Reshef, A.; Levin, G.; Kidron, D.; Cohen, A.; Ziv, I. Molecular imaging of cell death in vivo by a novel small molecule probe. *Apoptosis* **2006**, *11*, 2089–2101.

(10) Segers, J.; Laumonier, C.; Burtea, C.; Laurent, S.; Vander Elst, L.; Muller, R. N. From phage display to magnetophage, a new tool for magnetic resonance molecular imaging. *Bioconjugate Chem.* **2007**, *18*, 1251–1258.

(11) Shao, R.; Xiong, C.; Wen, X.; Gelovani, J. G.; Li, C. Targeting phosphatidylserine on apoptotic cells with phages and peptides selected from bacteriophage display library. *Mol. Imaging* **2007**, *6*, 417–426.

(12) Kettunen, M. I.; Brindle, K. M. Apoptosis detection using magnetic resonance imaging and spectroscopy. *Prog. Nucl. Magn. Reson. Spectrosc.* **2005**, *47*, 175–185.

(13) Blankenberg, F. In vivo detection of apoptosis. *J. Nucl. Med.* **2008**, *49*, 81S–95S.

(14) Ladner, R. C.; Sato, A. K.; Gorzelany, J.; de Souza, M. Phage display-derived peptides as therapeutic alternatives to antibodies. *Drug Discovery Today.* **2004**, *9*, 525–529.

(15) Wolters, S. L.; Corsten, M. F.; Reutelingsperger, C. P. M.; Narula, J.; Hofstra, L. Cardiovascular molecular imaging of apoptosis. *Eur. J. Nucl. Med. Mol. Imaging* **2007**, *34*, S86–S98.

past decade[16,17] in the context of theranostic approaches. However, the size of most atherosclerotic lesions is below the spatial resolution of nuclear or ultrasound imaging systems. Nuclear medicine has the advantage of superior sensitivity against low probe concentrations, but the targeted molecule could be roughly associated with a certain anatomic structure, in particular that related to the artery wall. In addition to the low anatomic resolution at larger penetration depths characterizing ultrasound imaging systems, the large size of ultrasound probes renders them less accessible to the targeted sites. The only clinical imaging technique able to attain a spatial resolution on the order of micrometers in a noninvasive way is MRI, which relies on the magnetic properties of ^{1}H, as one of the most abundant naturally occurring nuclei in the human body.[18,19] Even though the intrinsic MRI contrast is much more flexible than in other clinical imaging techniques, the diagnosis of several pathologies requires the involvement of CAs that can enhance the difference between normal and diseased tissues by modifying their intrinsic parameters. Paramagnetic (most of them complexes of gadolinium, known as positive contrast media) or superparamagnetic (generally consisting of iron oxides, known as negative agents) MR CAs are indirect agents because they do not become visible by themselves as opposed to other imaging modalities. The signal enhancement produced by MRI CAs (i.e., the efficiency of the CAs) depends on their longitudinal (r_1) and transverse (r_2) relaxivity (expressed in s^{-1} $mmol^{-1}$ L), which is defined as the increase of the nuclear relaxation rate (the reciprocal of the relaxation time) of water protons produced by 1 mmol per liter of CA.[17]

In the present work, a PS-specific 6-mer peptide identified by phage display technology was used to design an MRI CA that was evaluated as a potential *in vivo* reporter of apoptotic cells. After validation on a mouse model of liver apoptosis, the PS-targeted MRI CA was used to image atherosclerotic lesion on ApoE$^{-/-}$ transgenic mice. The provided data suggest thus that apoptosis-related pathologies could be diagnosed by MRI with a low molecular weight paramagnetic agent. Our paper represents to our knowledge the first proof of concept for the development of a CA with large and real perspectives for clinical applications. Moreover, the probe developed in the present work could be complexed with radioisotopes and then used in nuclear medicine, which has a superior sensitivity when compared to MRI.

2. Experimental Section

2.1. Phage Display Experiments. A library (fUSE5 vector)[20] of linear 6-mer (L6) random peptides displayed on all 5 copies of the pIII protein of M13 phage was used in this experiment. *Escherichia coli* host strain K91 BluKan is resistant to kanamycine, while the tetracycline resistance is transferred after infection with L6. The library and *E. coli* were kindly provided by Dr. Ulrichts from Catholic University of Leuven (Courtrai, Belgium).

L6 was screened during three rounds of panning against PS (1,2-dipalmitoyl-*sn*-glycero-3-phospho-L-serine, sodium salt, Genzyme Pharmaceuticals, Liesta, Switzerland), which was immobilized on microtiter plates. For immobilization, a solution of 0.083% PS was prepared in 95% ethanol (~80 °C, magnetic stirring), and 2 mL of this solution were poured in one well of a 6-well tissue culture plate. The ethanol was evaporated overnight, while PS formed a film at the bottom of the well. The well was then blocked with 3 mL of blocking buffer (4% Gloria milk powder, GMP, in TBS: 15.2 mM Tris-HCl, 150 mM NaCl, pH 7.5). After 2 h of incubation at 4 °C, the well was rinsed 6 times with TBS.

L6 (10^{13} phages in 0.5 mL of blocking buffer containing 0.4% GMP) was then incubated (2 h, room temperature) with a preblocked well (in the absence of PS) to remove phages that interact with plastic surface. L6 was then transferred to the PS coated well and incubated overnight at room temperature under mechanical agitation.

Nonbound phages were removed, and the well was rinsed 6 times with TBS. Bound phages were eluted (30 min, 1 mL of 0.1 M glycine, pH 2.0, room temperature, mild mechanical agitation), and the eluate was then neutralized with 250 μL of 1 M Tris-HCl, pH 8.0.

The next rounds of panning were performed as described above by using the amplified pool of the previous round of panning, with the following modifications: (1) phage number was reduced to 10^{12}, and (2) incubation times were diminished to 1 h for the nonspecific interaction with plastic surface and to 2 h for the interaction with PS.

Phages were amplified by infecting an *E. coli* culture when mid-log phase was attained (OD_{600} ~0.8−0.9). After 30 min of incubation at 37 °C, *E. coli* culture was spun 10 min at 2000 rpm. The pellet was suspended in 1 mL of 25 g/L LB (Luria−Bertani, Sigma-Aldrich, Bornem, Belgium) medium completed with 100 μg/mL kanamycin monosulfate (Kan, ICN, Asse-Relegem, Belgium) and 40 μg/mL tetracycline (Tet, Sigma-Aldrich). Aliquots of 250 μL were spread onto LB/Kan/agar (LB/Kan completed with 10 g of agar/L) Petri dishes. After overnight incubation at 37 °C, bacteria and phages were recovered with LB/Kan medium, then transferred into sterile tubes and spun 20 min at 8000 rpm and 4 °C. The supernatant was subsequently precipitated (2 h, 4 °C) with 1/5 cold PEG_{6000}/NaCl (20% polyethylene glycol 6000, 2.5 M NaCl), and then spun 20 min at 3200 rpm and

(16) Jaffer, F. A.; Libby, P.; Weissleder, R. Molecular and Cellular Imaging of Atherosclerosis - Emerging Applications. *J. Am. Coll. Cardiol.* **2006**, *47*, 1328–1338.

(17) Burtea, C.; Laurent, S.; Vander Elst, L.; Muller, R. N. Contrast Agents - Magnetic Resonance. In *Handbook of Experimental Pharmacology*, 185 Part 1; Semmler, W., Schwaiger, M., Eds.; Springer-Verlag: Berlin, Heidelberg, 2008; pp 135−165.

(18) Petersen, S. B., Muller, R. N., Rinck P. A., Eds. *An Introduction to Biomedical Nuclear Magnetic Resonance*; Thieme Verlag: Stuttgart, NY, 1985.

(19) Westbrook, C.; Kaut, C. *MRI in Practice*, 2nd ed.; Blackwell Publishing: Oxford, 1998.

(20) Smith, G.; Petrenko, V. A. Phage display. *Chem. Rev.* **1997**, *97*, 391–410.

4 °C. The pellet was suspended in 1 mL of sterile distilled water and reprecipitated with 1/5 cold PEG_{6000}/NaCl for 60 min at 4 °C. The tubes were then spun (5 min, 13,000 rpm, 4 °C), the supernatant discarded and the pellet suspended in 0.5 mL of TBS.

Individual phage clones were isolated by preparing 10-fold serial dilutions (dilution ranges: $10^{-3}-10^{-9}$) of the phage pool in LB/Kan. One hundred microliters of each phage dilution was used to infect (30 min, 37 °C) 900 μL of *E. coli* culture at mid-log phase. One at a time, the infected cells (100 μL) were transferred and spread carefully to one LB/Kan/agar/Tet plate and incubated overnight at 37 °C.

The phage clones were first amplified in microculture conditions by using a 96-well microculture plate; 200 μL of 2xYT/Kan/Tet culture medium (10 g of NaCl, 10 g of yeast extract, 16 g of tryptone, 100 μg of Kan/mL, 40 μg of Tet/mL) was inoculated with one colony of *E. coli* bearing one phage clone and incubated overnight at 37 °C under mild mechanical agitation. The microculture plates were then spun (15 min, 1000 rpm, 4 °C), and the supernatant of each well was transferred into sterile Eppendorf tubes.

2.2. Sequencing of the Selected Phage Clones. Phage DNA was isolated and purified by phenol extraction−ethanol precipitation. The sequence reaction (Mastercycler Personal Eppendorf, VWR International, Leuven, Belgium) was carried out by the Sanger method, using the Quick Start Kit (Beckman Coulter, Analis, Namur, Belgium) and an 18-base primer ($^{3'}$GGAGTATGTCTTTTAAGT$^{5'}$) (Invitrogen, Merelbeke, Belgium). DNA sequence was analyzed on a CEQ 2000 XL DNA Analysis System (Beckman Coulter). Sequence reading was performed automatically by using the JaMBW 1.1 software (http://bioinformatics.org/JaMBW/). Peptide sequences were aligned with BLAST (The Basic Local Alignment Search Tool).

2.3. Screening of the Affinity for PS and for Phosphatidylcholine of Isolated Phage Clones. Estimation of the Apparent Dissociation Constant (K^*_d). The preliminary screening of the affinity for PS or phosphatidylcholine (PC) (1,2-distearoyl-*sn*-glycero-3-phosphocholine, Genzyme Pharmaceuticals) of individual phage clones was evaluated by enzyme-linked immunosorbent assay (ELISA), using single phage concentration/clone to be analyzed. For this purpose, 50 μL volumes of the phage suspensions were incubated (2 h, 37 °C) with PS or PC (100 μg/mL, 200 μL/well) immobilized on ELISA plates. Among 306 initial clones, 21 were selected for sequencing and for the apparent dissociation constant (K^*_d) estimation. To obtain the titration curves for K^*_d, phage samples were diluted in Ca^{2+} buffer (2.5 mM $CaCl_2$, 150 mM NaCl, 10 mM Hepes, 3 mM NaN_3, pH 7.4). All washing steps were performed with Ca^{2+} buffer containing 0.5% Tween-20. Virions bound to the target were detected (1 h, room temperature) using 200 μL/well of horseradish peroxidase (HRP)-conjugated anti-M13 monoclonal antibody (Amersham Pharmacia Biotech Benelux, Roosendaal, The Netherlands) diluted to 1:5000 in the blocking buffer. The staining reaction was developed with 160 μL of HRP substrate solution containing 30 mL of 100 mM citric acid pH 2.0, 30 mL of 200 mM $Na_2HPO_4 \cdot 12H_2O$, 24 μL of 30% H_2O_2, and 600 μL of *o*-phenylenediamine dihydrochloride (Sigma-Aldrich, Bornem, Belgium). The reaction was stopped with 40 μL of 4 M H_2SO_4. The OD_{450} was measured using a microplate reader StatFax-2100 (Awarness Technology Inc., Fisher Bioblock Scientific).

2.4. Competition Test with AnnV. *2.4.1. Tests with Selected Phage Clones.* PS immobilized on microtiter plates was incubated (30 min, 37 °C) with various concentrations (2.73×10^{-7} M to 6.50×10^{-14} M) of AnnV (Sigma-Aldrich). The phage clone was then added at a concentration equal to its K^*_d for PS and incubated for 1 h at 37 °C. The subsequent steps of ELISA protocol are as described above. Data were used to estimate the half maximal inhibitory concentration (IC_{50}) of AnnV.

2.4.2. Tests with Selected Peptides. IC_{50} values were estimated for three selected peptides (PGDLSR, LIKKPF and DAHSFS) that were synthesized (NeoMPS, Strasbourg, France) and encoded as follows for simplicity: PGDLSR = R824, DAHSFS = R825, and LIKKPF = R826. Serial dilutions of peptides in Ca^{2+} buffer were incubated (30 min, 37 °C) with PS immobilized on microtiter plates. The competitor (biotinylated AnnV, AnnV-Bt, Sigma-Aldrich) was then added at a concentration equal to its K_d for PS (5×10^{-10} M) and incubated 1 h 30 min. After rinsing with Ca^{2+} buffer, AnnV-Bt bound to the target was detected (1 h, room temperature) with 200 μL of HRP-conjugated streptavidin (Sigma-Aldrich) diluted to 1:400. The staining reaction was developed with 200 μL/well of ABTS [2,2′-azino-bis(3-ethylbenz-thiazoline-6-sulfonic acid), diamonium salt (Sigma-Aldrich); 22 mg ABTS in 100 mL of 50 mM sodium citrate, pH 4.0] completed with 0.05% H_2O_2. OD_{405} values were measured using a microplate reader StatFax-2100.

2.5. Conjugation of the Selected PS Peptide Ligand and of Its Scrambled Homologue to Gd-DTPA (Gd-DTPA-g-R826, Gd-DTPA-g-R826.Sc). Physicochemical Characterization. For MRI evaluation on animal models of apoptosis, the PS-specific peptide LIKKPF (R826) and its scrambled homologue (FKIPKL, R826.Sc) were conjugated to Gd-DTPA (Gd-DTPA-g-R826 and Gd-DTPA-g-R826.Sc) (Scheme 1). The purity of the synthesized peptides ranged between >85% and >95% as determined by HPLC. In the case of MRI contrast agents, the purity was >95%.

Peptides with two Lys protected by trifluoroacetic acid and attached to 8-amino-3,6-dioxaoctanoyl were conjugated to 2 equiv of DTPA-isothiocyanate ((1-*p*-isothiocyanatobenzyl)-diethylenetriaminepentaacetic acid, Macrocyclics, Dallas, TX) in aqueous solution at a pH set between 8 and 9 (48 h, room temperature). Peptides were then unprotected with a saturated solution of K_2CO_3, and pH was adjusted to 7. The products were purified by dialysis on a Spectra/Por Biotech Cellulose Ester membrane with an MWCO of 500 (VWR, Leuven, Belgium) and by column chromatography on silica gel 60 RP-18 (40−63 μm) (Merck, Darmstadt, Germany) with methanol/water 40/60 (v/v) as elution solvent. For complexation, gadolinium chloride (1 equiv) was added (pH set between 6 and 8), and the solution was stirred 24 h. The presence of free

Scheme 1. Synthetic Scheme of Gd-DTPA Compounds

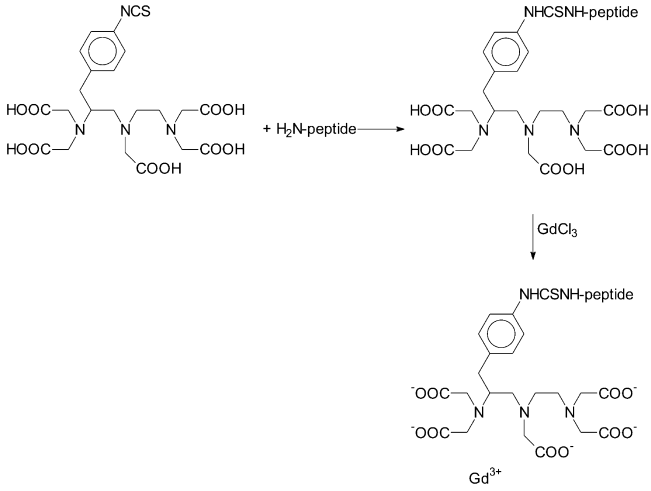

gadolinium ions was evaluated with arsenazo III. The complex was then dialyzed using a membrane with an MWCO of 500. Electrospray mass spectra were obtained on a Q-tof 2 (Micromass, Manchester, U.K.) in the positive ion mode at a capillary voltage of 3 kV. Ligand ESI-MS: $[M + H]^+$: 1431. Gd ESI-MS: $[M + H]^+$: 1586.

Proton nuclear magnetic relaxation dispersion (NMRD) profiles were recorded on a Stelar Relaxometer (Mede, Italy) working between 0.24 mT and 0.24 T. The additional relaxation rates at 0.47 T, 1.41 T, and 7.05 T were measured on mq-20 and mq-60 minispec systems (Bruker, Ettlingen, Germany), and on an AMX300 spectrometer (Bruker). The transmetalation measurements by Zn^{2+} ions were performed at 310 K and 0.47 T with a concentration of gadolinium complex and of Zn^{2+} ions of 2.5 mM, in a phosphate buffer ($[KH_2PO_4] = 0.026$ mol/L and $[Na_2HPO_4] = 0.041$ mol/L).[21]

2.6. Validation of the Affinity for Apoptotic Cells of Gd-DTPA-g-R826. Apoptosis was induced on Jurkat cells with 2 μM camptothecin (MP Biomedicals, Brussels, Belgium). Twenty-four hours later, apoptotic and control cells were resuspended in fresh culture medium at a concentration of 2×10^6 cells/mL. Four milliliters of this solution was incubated (2 h, room temperature, mechanical agitation) with Gd-DTPA-g-R826 (400 μM, 200 μM and 100 μM). Control samples were represented by nonapoptotic cells incubated with Gd-DTPA-g-R826, or by apoptotic and control cells incubated with nonspecific contrast agents Gd-DTPA-g-R826.Sc and Gd-DTPA. Subsequently, the cells were centrifuged (4500 rpm, 15 min) and rinsed 3 times with 4 mL of Ca^{2+} buffer. The cell pellet was mineralized with 0.8 mL of nitric acid in a water bath at 80 °C for 4 h. Gd concentration was evaluated by inductively coupled plasma-mass spectroscopy (ICP-MS, ELAN-6100, Perkin-Elmer, Courtaboeuf, France).

2.7. In Vivo MRI Evaluation of Gd-DTPA-g-R826. The *in vivo* MRI evaluation was carried out on a mouse model of liver apoptosis ($n = 54$) induced by anti-Fas antibody (purified hamster antimouse Fas monoclonal antibody, clone Jo2, isotype $\lambda 2$, BD Biosciences Pharmingen, Erembodegem, Belgium)[25] and on transgenic female C57bl/6 ApoE^{tm1unc} (ApoE$^{-/-}$) mice ($n = 20$). Prior to MRI scans, animals were anesthetized with 50 mg/kg of sodium pentobarbital (Nembutal, Sanofi, Brussels, Belgium). All animal experiments were conducted in accordance with the requirements of the Ethical Committee of our institution. Images were acquired before and after injection of CAs on a 4.7 T Bruker imaging system (Bruker) equipped with a vertical magnet and a microimaging device (Micro2.5AHS/RF, 25 mm coil).

2.7.1. MRI of Liver Apoptosis. Liver apoptosis was induced in Balb/c mice (27 ± 1.86 g, Harlan, Horst, The Netherlands) by iv (caudal vein) injection of anti-Fas antibody at a dose of 10 μg/25 g.[25] Before injecting anti-FAS, animals were anesthetized with 50 mg/kg bw, ip of Nembutal diluted to 1:5 with physiological salt. The time schedule of MRI sessions was the following: (1) precontrast MRI session started 1 h 15 min after anti-Fas injection; (2) contrast agents were injected iv (caudal vein) at a dose of 0.06 mmol/kg bw ~1 h 45 min after anti-Fas injection; (3) several postcontrast MRI acquisitions were performed for ~1 h 30 min. Competition experiments were performed with peptide R826, which was injected iv (0.1 mmol/kg bw) ~10 min before Gd-DTPA-g-R826.

Images were acquired with an MSME (Multi-Slice Multi-Echo) T_1-weighted MRI sequence [TR/TE = 307.4/14.7 ms, number of echoes = 1, matrix = 256, number of averages = 4, FOV = 5 cm, slice thickness = 3 mm, 8 axial slices, spatial resolution = 195 μm, TA = 5 min 14 s].

Signal intensity (SI) was measured in regions of interest (ROIs) covering the whole liver and in a region placed outside the animal's image (Noise) by using OSIRIS image analysis software, and average SI enhancement (SIE) (ΔSNR%) was calculated according to the following equation:

(21) Laurent, S.; Vander Elst, L.; Copoix, F.; Muller, R. N. Stability of MRI paramagnetic contrast media. A proton relaxometric protocol for transmetallation assessment. *Invest. Radiol.* **2001**, *36*, 115–122.

(22) Laurent, S.; Botteman, F.; Vander Elst, L.; Muller, R. N. Relaxivity and transmetallation stability of new benzyl-substituted derivatives of gadolinium-DTPA complexes. *Helv. Chim. Acta* **2004**, *87*, 1077–1089.

(23) Muller, R. N.; Radüchel, B.; Laurent, S.; Platzek, J.; Piérart, C.; Mareski, P.; Vander Elst, L. Physicochemical characterization of MS-325, a new gadolinium complex, by nuclear relaxometry. *Eur. Inorg. Chem.* **1999**, 1949–1955.

(24) Henoumont, C.; Henrotte, V.; Laurent, S.; Vander Elst, L.; Muller, R. N. Synthesis of a new gadolinium complex with a high affinity for human serum albumin and its manifold physicochemical characterization by proton relaxation rate analysis, NMR diffusometry and electrospray mass spectrometry. *J. Inorg. Biochem.* **2008**, *102*, 721–730.

(25) Blankenberg, F. G.; Katsikis, P. D.; Tait, J. F.; Davis, R. E.; Naumovski, L.; Ohtsuki, K.; Kopiwoda, S.; Abrams, M. J.; Strauss, H. W. Imaging of apoptosis (programmed cell death) with 99mTc Annexin V. *J. Nucl. Med.* **1999**, *40*, 184–191.

$$\Delta SNR\% = \frac{[SI_{post}/(Noise\ SI)] - [SI_{pre}/(Noise\ SI)]}{[SI_{pre}/(Noise\ SI)]} \times 100$$

where SI_{post} = postcontrast SI and SI_{pre} = precontrast SI.

2.7.2. MRI of Atherosclerosis. Female ApoE$^{-/-}$ mice, aged ~15 months, were fed on a Western diet for three months before MRI experiments. CAs were injected iv at a dose of 0.1 mmol/kg bw. Images were acquired as previously described[26] at the level of the abdominal aorta with RARE (rapid acquisition with relaxation enhancement) imaging protocol (TR/TE = 1048.5/4 ms, RARE factor = 4, NEX = 4, matrix = 256, FOV = 2.3 cm, slice thickness 0.8 mm, 20 axial slices, spatial resolution = 90 μm, TA = 4 min 28 s). A 3D-TOF (time-of-flight) sequence (TR/TE = 10/2 ms, flip angle = 20°, NEX = 2, FOV = 4 × 2 × 4 cm, matrix = 256 × 128 × 64, slice thickness = 1 mm, 60 axial slices, spatial resolution = 156 × 156 × 625 μm, TA = 2 min 43 s) was used with the aim of confirming the anatomical localization of the aorta in the image slice.

SI values for each time point were measured within ROIs drawn manually by using the OSIRIS image analysis software in the arterial wall of the abdominal aorta. The ROIs were drawn on serial slices on the area of signal enhancement around the vessel lumen and were reproduced for precontrast images, where the aortic wall was not discriminated from the surrounding tissue. The standard deviation (SD) of noise was also measured in a region situated out of the animal's image. The superior anatomical resolution of atherosclerotic plaque obtained with RARE imaging sequence was associated with higher SI values of the noise. Thus, only SD values of the noise were pertinent for an objective calculation of SNR. ΔSNR% was calculated according to the following equation:

$$\Delta SNR\% = \frac{[SI_{post}/(Noise\ SD)] - [SI_{pre}/(Noise\ SD)]}{[SI_{pre}/(Noise\ SD)]} \times 100$$

The ΔSNR% data were averaged and the standard error of the mean (SEM) was calculated for each time point.

2.8. Confirmation of Apoptosis in Biological Models. *2.8.1. Enzymatic Activity of Caspase-3 in Jurkat Cell Samples.* After induction of apoptosis as described above, enzymatic activity of caspase-3 was assessed on Jurkat cell samples by using caspase colorimetric QuantiPak kit (Tebu-Bio, Boechout, Belgium) according to the manufacturer's protocol.

2.8.2. Immunohistochemistry. 2.8.2.1. Identification of Apoptotic Jurkat Cells with AnnV-Bt. Apoptotic Jurkat cells were immunostained after treatment with camptothecin by incubation (2 × 10^6 cells/mL) with 5 μL/mL of AnnV-Bt (Fisher Bioblock Scientific, Tournai, Belgium) for 30 min at room temperature, followed by two times rinsing with 1 mL of Ca^{2+} buffer. Before incubation with AnnV-Bt, endogenous peroxidases were blocked with 0.06% H_2O_2, while endogenous biotin was blocked with a blocking kit (Invitrogen). Cells labeled with AnnV-Bt were immobilized on poly-L-Lys (Invitrogen) coated coverslips and fixed (15 min, room temperature) with 2 mL of 4% buffered paraformaldehyde (PAF). After incubation with streptavidin-linked peroxydase complexes (ABC kit, DakoCytomation SAS, Trappes, France), the samples were incubated 5 min with 50 mM Tris-HCl, pH 7.4, and then stained with 0.05% 3,3′-diaminobenzidine (DAB) completed with 0.02% H_2O_2 in PBS. Cells were counterstained with Luxol fast blue and mounted in a permanent medium.

2.8.2.2. Detection of Apoptotic Cells in Liver and Aorta. 2.8.2.2.1. Immunohistochemistry of PS. After rinsing in cold PBS solution, the organs (aorta and liver) were weighed and transferred into cold Ca^{2+} buffer completed with AnnV-Bt. After 1 h of incubation at 4 °C, the samples were rinsed 4 times with Ca^{2+} buffer (12 mL/sample). They were then fixed in a solution of 4% formalin in Ca^{2+} buffer completed with 3 mM NaN_3 and adjusted to pH 7.4. Fixed tissue specimens were rinsed in 70% ethanol, progressively dehydrated in graded ethanol solutions and in butanol, and embedded in Paraplast Plus paraffin. Then, 5 μm thick sections were cut, dewaxed, and rehydrated. Endogenous peroxidases were blocked with 0.15% H_2O_2, whereas nonspecific epitopes were blocked with protein-free blocking buffer (PFBB, Perbio Science, Erembodegem, Belgium). AnnV-Bt was detected with goat antibiotin IgG (5 μg/mL) and horse peroxidase-conjugated antigoat IgG (1 μg/mL) (both from Vector Labconsult, Brussels, Belgium). Staining was developed with DAB, and sections were counterstained with hemalun and Luxol fast blue as described above.

2.8.2.2.2. Immunohistochemistry of Caspase-3. The aorta samples were fixed in a solution of Bouin's/Duboscq Brazil and the liver samples in one of buffered 4% PAF. They were then embedded in paraffin, and 5 μm thick sections were cut. After dewaxing and rehydration, the antigen was retrieved with citrate buffer, pH 6.0 (20 min, 95−100 °C); endogenous peroxidases, biotin, and nonspecific epitopes were blocked as described above. The sections were then incubated overnight with cleaved caspase-3 rabbit monoclonal antibody (Cell Signaling, Bioké, Leiden, The Netherlands) diluted to 1:50 for aorta and to 1:100 in the case of liver. Sections were then incubated with 5 μg/mL (liver) or 10 μg/mL (aorta), respectively, of biotinylated goat antirabbit IgG (Vector Labconsult). Subsequently, aorta sections were incubated with goat antibiotin IgG (5 μg/mL) and horse peroxidase-conjugated antigoat IgG (1 μg/mL); in the case of liver, the sections were incubated with streptavidin-linked peroxydase complexes. Staining, counterstaining, and mounting were performed as described above.

(26) Burtea, C.; Laurent, S.; Murariu, O.; Rattat, D.; Toubeau, G.; Verbruggen, A.; Vansthertem, D.; Vander Elst, L.; Muller, R. N. Molecular imaging of $\alpha_v\beta_3$ integrin expression in atherosclerotic plaques with a mimetic of RGD peptide grafted to Gd-DTPA. *Cardiovasc. Res.* **2008**, *78*, 148–157.

3. Results

3.1. Characterization of the Candidate Phage Clones. *3.1.1. Validation of Candidate PS Peptide Ligands.* The *in vitro* screening of a linear 6-mer random peptide library against immobilized PS allowed for the selection of 56 phage clones presenting high affinity for the target. The affinity for PC, which is another major phospholipid of cell membranes, was also evaluated and compared to the affinity for PS. The ratio affinity for PS versus PC ranged from 0.6 up to 2.9, with a mean of 1.8 and a variance of 0.5. This result indicated that all clones have an affinity for PC, although for most of them this affinity was inferior to that for PS. Twenty-one peptide clones presenting a ratio >1.8 were thus selected for further characterization.

3.1.2. Peptide Sequence of the Selected PS-Binding Clones. The most frequently represented peptides among the 21 sequenced phage clones are PGDLST and DAHSFS (Table 1). Apart from VLGREG and LIKKPF, the other peptides have consensus motifs represented by DAHS and GDL, which could be essential for PS binding. Peptide homology with sequence of relevant proteins is also shown in Table 1.

Amino acid frequency in the peptide structure is represented in Figure 1A. One can notice that L, S, G and D are the most frequent amino acids, while P, T and H are quite well represented. Amino acids S, T, D and H are polar, either ionizable (D and H) or not (S and T), and they can contract an ionic or hydrogen interaction with the polar head of PS.[27,28] Amino acids L and G may stabilize the interaction with PS by a hydrophobic association.[28]

3.1.3. Estimation of K^*_d of the Phage Clones for PS. Comparative Affinity for PC. The K^*_d values designate peptides PGDLSR, LIKKPF and DAHSFS as presenting the highest affinity for PS (Figure 1B). PGDLSR and LIKKPF have a higher affinity for PS than for PC (Figure 1C) whereas DAHSFS does not.

3.1.4. Competition Experiments with AnnV. The competition with AnnV was carried out for the phage-peptide clones PGDLSR, LIKKPF and DAHSFS.

IC_{50} of AnnV was quite similar (1.08×10^{-9} M for LIKKPF, 1.31×10^{-9} M for DAHSFS, and 1.38×10^{-9} M for PGDLSR) and about 2 times higher than its own K_d for PS ($\sim 5 \times 10^{-10}$ M for human recombinant AnnV).[33] In other words, a concentration of AnnV equal to $2 \times K_d^{AnnV}$ is necessary to remove peptides from their binding sites.

The ratio between IC_{50} of AnnV and the peptide clone's K^*_d (Figure 1D) indicates PGDLSR as the stronger peptide ligand, since AnnV concentration required to inhibit by 50% its interaction with PS is ~1.2 times higher than its K^*_d. DAHSFS seems to be the weaker PS-binding peptide because its dissociation from the binding sites occurs at an AnnV concentration ~50% lower than its K^*_d for PS.

3.1.5. Characterization of the Candidate PS-Specific Peptide Ligands. 3.1.5.1. Theoretical Biochemical Parameters of the Three Candidate Peptides R824, R825 and R826. The characterization of the PS-specific phage clones evidenced peptides PGDLSR (R824), DAHSFS (R825) and LIKKPF (R826) (Figure 2) as the most important PS ligands based on their specific affinity for PS. These peptides were selected for subsequent *in vitro* and eventual *in vivo* evaluation after their synthesis.

Some of the biochemical parameters of these peptides were theoretically estimated by using the tools of the ExPASy Proteomics Server and ACDLabs 12.0 software (Table 2). The predicted half-life is based on the N-end rule[29] and shows that peptide R824 has the longest half-life (>20 h), followed by R826 (5.5 h) and R825 (1.1 h). However, when compared to the instability index,[30] an optimal behavior could be noticed for peptide R826 which is relatively stable (instability index <40), while its half-life (based on the probability of intracellular ubiquitin mediated degradation) could be reasonable for the time-window of an MRI scanning if the peptide is used for diagnosis purposes after conjugation to a magnetic reporter; in contrast, peptide R824 is predicted as unstable (instability index = 40.43).

The p*I* indicates that the three candidate peptides are ionized at physiological pH (pH 7.4), which suggests that their interaction with the polar head of PS is possible. The aliphatic index,[31] which is moreover an index of thermostability, points out again the peptide R826 as having the most important composition in aliphatic amino acids. This may contribute to the hydrophobic association with the membrane of apoptotic cells in addition to its positive charge conferred by the two Lys. The LogP and GRAVY[32] show both that peptide R826 has a certain hydrophobic character when compared to the two other peptides, which may play a role in the interaction with apoptotic cells.

3.1.5.2. In Vitro Evaluation: Estimation of Peptide IC_{50} in Competition with AnnV. IC_{50} was estimated for the synthesized

(27) Montaville, P.; Neumann, J.-M.; Russo-Marie, F.; Ochsenbein, F.; Sanson, A. A new consensus sequence for phosphatidylserine recognition by annexins. *J. Biol. Chem.* **2002**, *277*, 24684–24693.

(28) Lesk, A. M. *Introduction to Protein Science*; Oxford University Press: New York, 2006; pp 73−85.

(29) Bachmair, A.; Finley, D.; Varshavsky, A. In vivo half-life of a protein is a function of its amino-terminal residue. *Science* **1986**, *234*, 179–186.

(30) Guruprasad, K.; Reddy, B. V. B.; Pandit, M. W. Correlation between stability of a protein and its dipeptide composition: a novel approach for predicting in vivo stability of a protein from its primary sequence. *Protein Eng.* **1990**, *4*, 155–161.

(31) Ikai, A. J. Thermostability and aliphatic index of globular proteins. *J. Biochem.* **1980**, *88*, 1895–1898.

(32) Kyte, J.; Doolittle, R. F. A simple method for displaying the hydropathic character of a protein. *J. Mol. Biol.* **1982**, *157*, 105–132.

(33) Andree, H. A.; Reutelingsperger, C. P.; Hauptmann, R.; Hemker, H. C.; Hermens, W. T.; Willems, G. M. Binding of vascular anticoagulant α (VACα) to planar phospholipid bilayers. *J. Biol. Chem.* **1990**, *265*, 4923–4928.

Table 1. Peptide Sequences and Their Frequency among the Selected Phage Clones[a]

Peptide sequence (No. of clones)	Relative homology with sequence of relevant proteins
DAHSF**S** (5)	Human Ca^{2+} channel voltage-dependent, T-type α-1H subunit (AN: 095180; extracellular domain : D^{389}-A-H-S-F^{394})
DAHS**LS** (1)	Human proto-oncogene Tyr-protein kinase Src (AN: P12931; SH3 domain: A^{124}-H-S-L-S^{128}) Mouse neuronal proto-oncogene Tyr-protein kinase Src (AN: P05480; SH3 domain: A^{129}-H-S-L-S^{133})
PGDL**ST** (7)	Human matrix metalloproteinase-14 (AN: P50281; (activation peptide: P^{47}-G-D-L-*R*-T^{52}; extracellular domain: G^{187}-D-Gap-S-T^{190}) and metalloproteinase-9 (AN: P14780; activation peptide: P^{32}-G-D-L-*R*-T^{37}) Mouse matrix metalloproteinase 14 (AN: P53690; extracellular domain: G^{187}-D-S-T^{190}) Fas-binding factor 1 (AN: Q8TES7; P^{518}-G-D-L-S^{522})
PGDL**SR** (3)	Rat transient receptor potential Ca^{2+} channel 6C (AN: Q99N76; P^{300}-G-D-L-*A*-R^{305}) Rabbit acyl-coenzyme A oxydase 2 peroxisomal (AN: O02767; P^{192}-G-D-L-*G*-R^{197}) Fas-binding factor 1 (AN: Q8TES7; P^{518}-G-D-L-S^{522})
PGDLV**R** (1)	Rat transient receptor potential Ca^{2+} channel 6B (AN: Q99N77; P^{300}-G-D-L-*A*-R^{305}) Rat fas antigen ligand (AN: P36940; extracellular domain: P^{216}-G-D-L-V^{220})
HGDL**ST** (1)	Mouse K^+ inwardly-rectifying channel (AN: P35561; extracellular domain: H^{110}-G-*D*-L-D-T^{115}) Human ATP-sensitive inward rectifier K^+ channel 14 (AN: Q9UNX9; extracellular domain: H^{115}-G-D-L^{118})
HG**H**L**S**I (1)	Human protein Tyr phosphatase 2C (AN: Q06124; SH2 2 domain: H^{114}-G-H-L-S^{118}) Human alanine:glyoxylate aminotransferase 2-like 1 (AN: Q8TBG4; H^{140}-G-H-L-S^{144})
VLGE**R**G (1)	Mouse apoptosis associated Tyr-kinase (AN: Q80YE4; V^{140}-*F*-L-G-E^{144}) Rat Ca^{2+} channel β-subunit 3B (AN: Q9QVV3; L^{378}-G-E-R-G^{182})
LIKK**P**F (1)	Human transient receptor potential Ca^{2+} channel 5 (AN: Q9UL62; extracellular domain: L^{358}-*F*-I-K-K-P-F^{364}) Mouse capacitative Ca^{2+} entry channel 2 (AN: Q9QX29; extracellular domain: L^{358}-*F*-I-K-K-P-F^{364})

[a] Alignment with relevant protein sequences (identified with Swiss-Prot accession numbers, AN) and the homologous amino acids are also shown. The frequent motifs (gray boxes) and amino acids (bold underlined) are highlighted. The BLAST search revealed that some of the peptide sequences are homologous with many other proteins that are pertinent to the present work, but they were not included in Table 1 in order to save editorial space.

peptides in competition with AnnV-Bt (Figure 3A−C). Their IC_{50} indicated peptide R824 as the most efficient competitor of AnnV, followed by R826 and R825. The ratio IC_{50}/K^*_d reflects the concentration of peptides

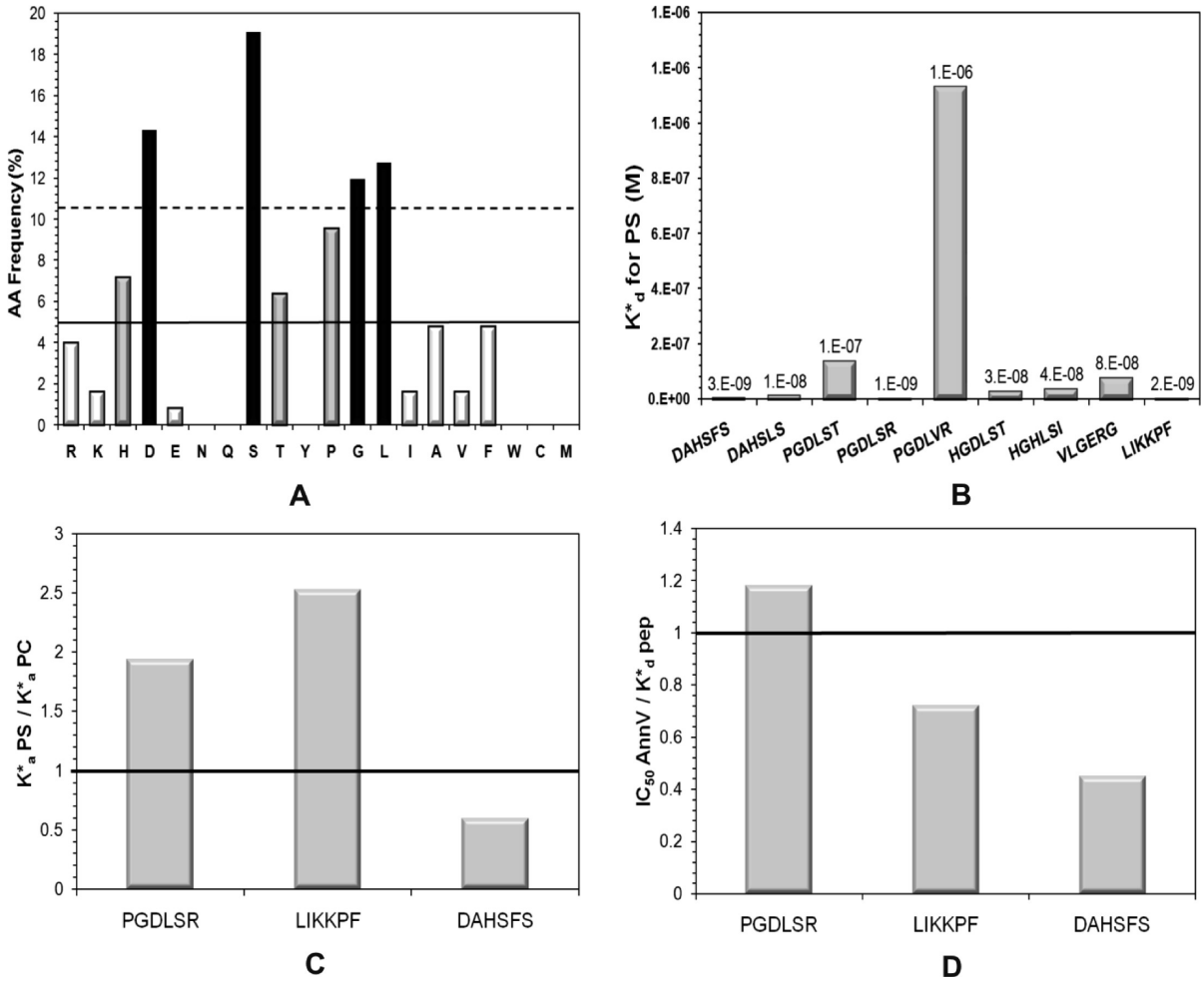

Figure 1. Amino acid composition of the selected phage clones and their specific affinity for PS. (A) Amino acid frequency in peptide structure. Solid line represents the mean; dotted line represents the mean + variance. (B) K^*_d for PS of 9 identified PS peptide ligands. (C) Comparative affinity for PS and for PC of peptide clones PGDLSR, LIKKPF and DAHSFS. Results are represented as a ratio K^*_a for PS/K^*_a for PC. (D) Ratio between IC_{50}^{AnnV} and K^*_d of three PS-specific peptide clones.

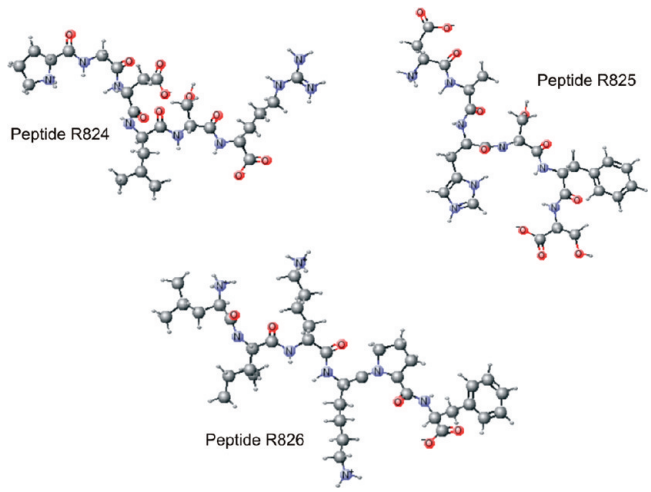

Figure 2. 3D chemical structure of the three PS-specific candidate peptides at physiological pH.

Table 2. Theoretical Biochemical Parameters of the Three Candidate Peptides R824, R825 and R826, Respectively, as Estimated by Using ExPASy Proteomics Server, Proteomics and Sequence Analysis Tools[a]

parameter[b]	R824	R825	R826
half-life	>20 h	1.1 h	5.5 h
instability index	40.43	−5.82	13.72
p*I*	6.27	5.08	10.00
LogP	−2.33 ± 0.86	−1.79 ± 0.88	2.51 ± 0.86
GRAVY	−1.167	−0.617	0.283
aliphatic index	65	16.67	130

[a] LogP was calculated by using the ACDLabs 12.0 software. [b] Half-life: theoretically estimated in mammalian reticulocytes *in vitro*. Instability index: when smaller than 40, the protein (or peptide) is predicted as stable. p*I* = isoelectric point. LogP = partition coefficient. GRAVY = grand average of hydropathicity (predicts the hydrophobicity). Aliphatic index = the relative volume occupied by aliphatic side chains.

required to dissociate AnnV from binding sites in relation to the K^*_d values estimated for corresponding clones (Figure 3D). R826 was thus highlighted as the most powerful PS-specific peptide and selected to be conjugated to Gd-DTPA (Gd-DTPA-g-R826). The scrambled se-

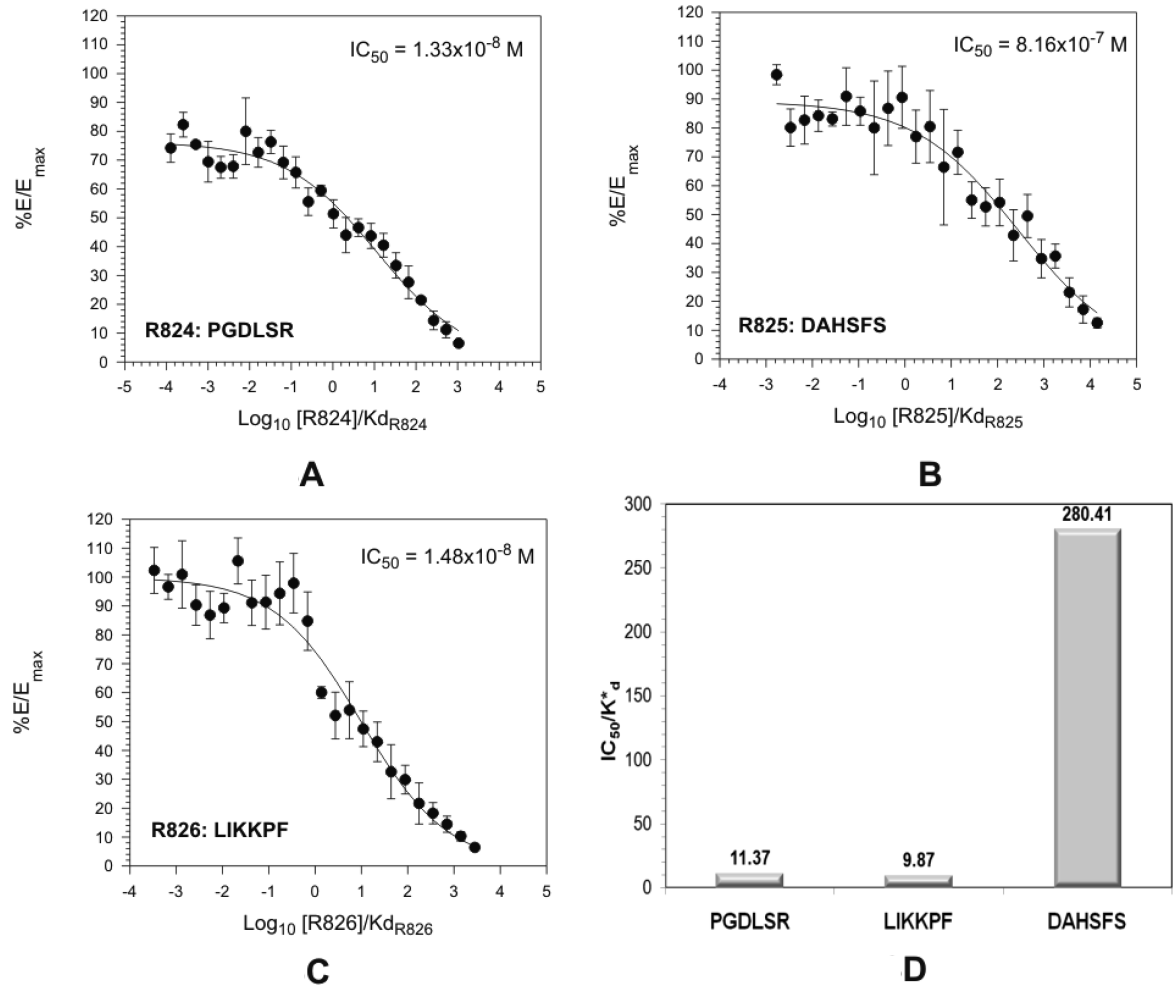

Figure 3. Specific affinity for PS of the synthesized peptides. (A−C) IC_{50} of R824, R825, and R826 determined in competition with AnnV-Bt. (D) Ratio IC_{50}/K^*_d for PS-specific peptides.

quence of the same peptide (R826.Sc) was also conjugated to Gd-DTPA (Gd-DTPA-g-R826.Sc) and it served as a nonspecific control compound.

3.1.5.3. Physicochemical Characterization of Gd Complexes. The new Gd complexes (Gd-DTPA-g-R826 and Gd-DTPA-g-R826.Sc) show similar and larger relaxivity when compared to that of the parent compound, Gd-DTPA (Figure 4A). Transmetalation experiments show higher stability for R826-vectorized complexes in comparison to Gd-DTPA (Figure 4B). This increase of the stability seems to be a common feature for Gd-DTPA derivatives substituted in the C-4 position of the backbone.[21−24]

3.1.5.4. Validation of the Affinity for Apoptotic Cells of Gd-DTPA-g-R826. The binding of Gd-DTPA-g-R826 to apoptotic cells was evaluated on Jurkat T lymphocytes (Figure 5A). Higher concentrations of Gd-DTPA-g-R826 found in apoptotic samples ($p < 0.01$) as compared to those in various controls plead for a specific interaction with PS. The level of binding to apoptotic cells is ∼3 times higher than that to control cells, and 5100 to ∼10,000% superior to nonspecific compounds Gd-DTPA-g-R826.Sc and Gd-DTPA.

Apoptosis was confirmed in cell samples with AnnV-Bt (Figure 5B) and by the measurement of caspase-3 activity, which indicated ∼10 times higher enzymatic activity for apoptotic samples (613 ± 66 pmol/min) in comparison to control cells (67 ± 9 pmol/min).

3.1.5.5. In Vivo MRI Evaluation of Gd-DTPA-g-R826 on a Mouse Model of Liver Apoptosis. The potential of Gd-DTPA-g-R826 to identify apoptotic cells *in vivo* by MRI was first validated on a mouse model of liver apoptosis.

Gd-DTPA-g-R826 enhanced the SI at the level of liver parenchyma within minutes (∼7 min) following injection. This enhancement showed a patchy distribution and was superior (Figure 6A) to that produced by conventional Gd-DTPA (Figure 6D).

The specific uptake of Gd-DTPA-g-R826 in apoptotic livers was validated by preinjecting R826, which attenuated the positive contrast (Figure 6B).

Gd-DTPA-g-R826 yielded a minimal SIE in healthy mice (Figure 6C), which was not significantly different from that of Gd-DTPA (Figure 6E).

Gd-DTPA-g-R826.Sc had a rather homogeneous distribution in apoptotic liver and its retention was reduced in comparison with Gd-DTPA-g-R826 (Figure 6F).

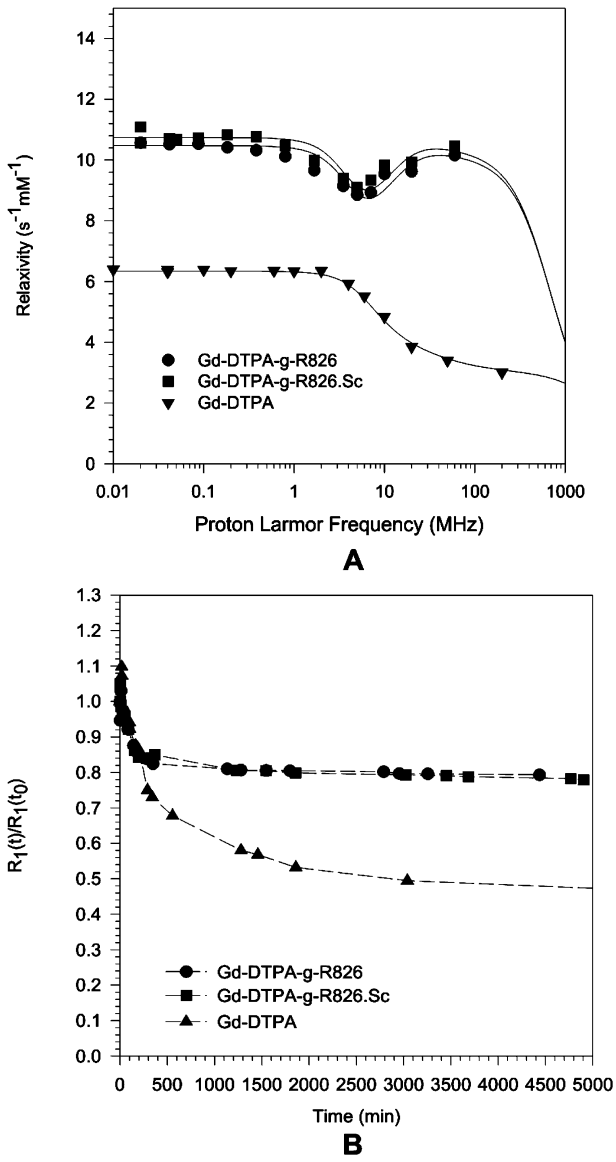

Figure 4. Physicochemical characterization of Gd-DTPA-g-R826 and of Gd-DTPA-g-R826.Sc. (A) NMRD profiles at 310 K in comparison with Gd-DTPA. (B) Evolution of the paramagnetic proton relaxation rate during transmetalation.

Apoptosis was confirmed on liver specimens by immunostaining of PS with AnnV-Bt (Figure 6G) and of active caspase-3 with a specific antibody (Figure 6H).

ΔSNR% measured on liver images is represented in Figure 7. In apoptotic livers, Gd-DTPA-g-R826 enhanced ΔSNR% progressively up to 94% 1 h postcontrast, and then decreased to 60% at the end of the MRI session. SI in healthy livers increased to 38% 8 min postcontrast, then constantly diminished and did not surpass the SI produced by Gd-DTPA.

The competition with R826 depressed ΔSNR% in apoptotic livers to a range close to that in healthy livers, with a tendency to increase until 39% 77 min postcontrast.

Gd-DTPA-g-R826.Sc enhanced the SI of apoptotic livers to ∼40%, which remained almost constant during the MRI scanning period; SI of healthy livers was comparable to that of the two other CAs.

These results suggest that most of the increased liver localization of Gd-DTPA-g-R826 is the result of a specific interaction with apoptotic hepatocytes. The nonspecific accumulation due to the disruption of hepatic blood vessels in this acute model of apoptosis is possible, but this might have a lesser contribution as proven by the results obtained with the other experimental groups.

3.1.5.6. MRI of Apoptotic Cells in a Mouse Model of Atherosclerosis (ApoE$^{-/-}$). Imaging of apoptotic cells in atherosclerotic plaques was assessed on ApoE$^{-/-}$ mice. In precontrast images, the artery wall is hardly visible (Figure 8a) and cannot be differentiated from the surrounding tissue, whereas in postcontrast images obtained with Gd-DTPA-g-R826 (Figure 8b) it is possible to distinguish the anatomical details of the artery wall. The slight mismatch between the pre- and the postcontrast images is due to the repositioning of the animal after the administration of the contrast agent and the darkening of the kidneys results from a T_2 effect induced by a high renal concentration of the compound. The anatomic slices are thus almost in the same position, taking into account the spine as a reference (the other organs change relatively their position). The images obtained with TOF imaging protocol (Figure 8c) also show satisfactory plaque delineation after the injection of Gd-DTPA-g-R826, which corresponded to plaque SIE in RARE images. Gd-DTPA only produced a slight SIE (Figure 8d) allowing limited plaque demarcation from the surrounding tissues. Literature reports that plaque microvessels may be relatively permeable, and Gd-based CAs could enhance areas rich in plaque microvascularization.[15] Gd-DTPA-g-R826.Sc produced a diminished plaque SIE (Figure 8f) when compared to Gd-DTPA-g-R826 (Figure 8e), but the signal was not completely abolished. This is probably explained by the free diffusion of CA through the aortic wall, which is facilitated by the high blood pressure in this major artery of the circulatory system.

Serial image slices of abdominal aorta obtained 30 min post Gd-DTPA-g-R826 (Figure 9a) were compared to SIE yielded by Gd-DTPA (Figure 9b), which clearly did not ensure a convenient plaque distinction from the neighboring tissues. The shape of atherosclerotic plaque is rather heterogeneous, implying that the artery wall (on its length and circumference) is not completely modified by the lesion.

Immunohistochemistry for PS (Figure 9c,d) and caspase-3 (Figure 9e) on aorta specimens harvested after MRI studies confirmed the presence of apoptotic cells in atherosclerotic plaques. AnnV-Bt was captured in the disorganized tunica media (Figure 9c) and in the head (Figure 9d) of plaques that cover large fatty/necrotic cores.

Measurement of ΔSNR% on RARE images (Figure 9f) confirms the high SI of the aortic wall enhanced by Gd-DTPA-g-R826. This was maximal (132%) 11 min postcontrast, but remained enhanced (111%) until 61 min, when the imaging experiment was finished. SI enhanced by Gd-DTPA-R826.Sc was less important and did not surpass 93% (25

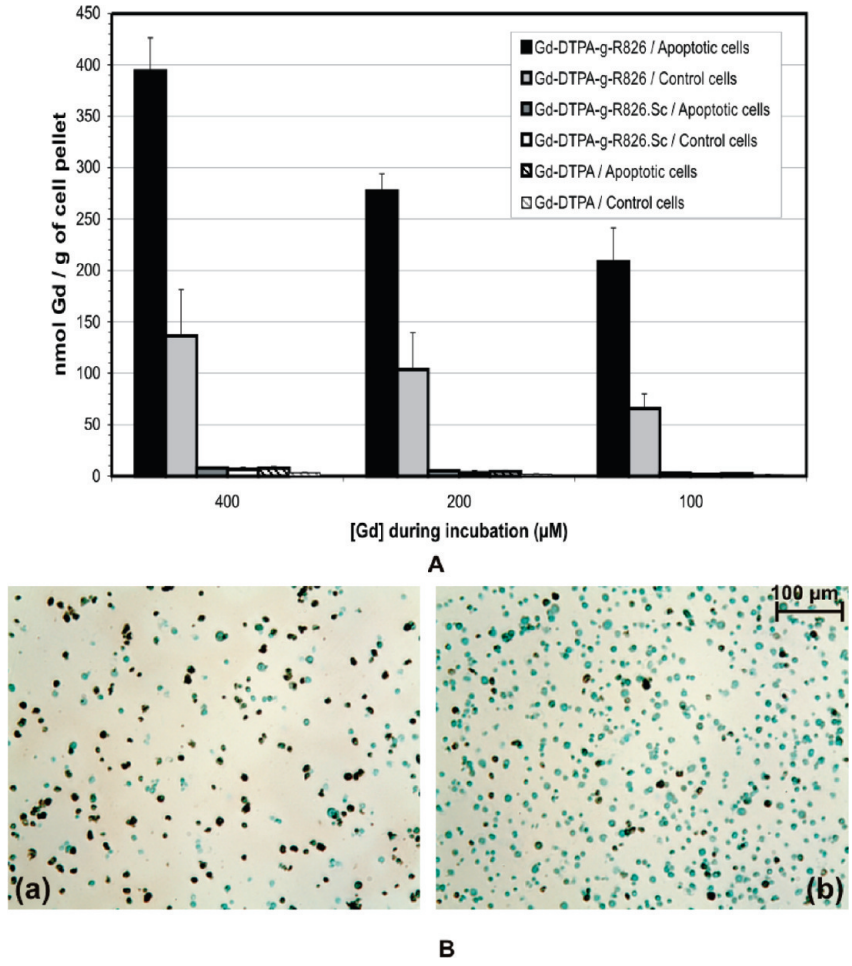

Figure 5. Binding of Gd-DTPA-g-R826 to apoptotic Jurkat cells as compared to various controls. (A) Gd concentration in apoptotic and control cell samples; 73 ± 11% dead cells in apoptotic samples, 12 ± 3% dead cells in control samples (Trypan blue exclusion assay). (B) Apoptotic cells were stained (brown) in camptothecin treated (a) and control (b) samples with AnnV-Bt.

min postcontrast), having a level of 68% at 60 min. ΔSNR% produced by Gd-DTPA ranged between 89% and 45%.

4. Discussion and Conclusions

Phage display technology has allowed us to identify peptides targeted to PS exposed by apoptotic cells, which could assist the diagnosis of vulnerable atherosclerotic plaques by molecular imaging. This biomolecule involved in the mechanism of atherothrombosis represents one of the most important imaging targets in atherosclerosis. At the same time, it is important to highlight that ApoE$^{-/-}$ mouse used in our experiments is a very useful model to study the expression and targeting of various biomolecules characteristic to atherosclerosis, but the manifestations of plaque vulnerability and disruption in mice differ from those in humans. In apoE$^{-/-}$ and LDLR$^{-/-}$ mice, plaque ruptures occur predominantly in the brachiocephalic artery, but they seem to be less frequent than in humans. Plaque instability mainly takes the form of erosion and intraplaque bleeding without thrombus formation. Repeated erosions have been assumed to cause lesion growth and may contribute to the development of lesions with multiple caplike structures.[34]

The screening against immobilized PS allowed for the selection of 21 candidate phage clones as potentially selective binders based on their preference for this phospholipid as compared to PC.

The sequencing of their genome highlighted 9 different peptides, with PGDLST and DAHSFS being the most frequently represented. Only one phage clone expressed peptide LIKKPF and no other peptide motifs were related to this one.

Peptide alignment with relevant proteins revealed a frequent correspondence with that of Ca^{2+} channels, which is reminiscent of the function of annexins that are Ca^{2+}-dependent phospholipid binders and mediators of intracellular Ca^{2+} signal.[35] Although a matter of some debate, the function of annexins as ion channel proteins has been broadly investigated by attempting to elucidate its molecular

(34) Schwartz, S. M.; Galis, Z. S.; Rosenfeld, M. E.; Falk, E. Plaque Rupture in Humans and Mice. *Arterioscler. Thromb. Vasc. Biol.* **2007**, *27*, 705–713.

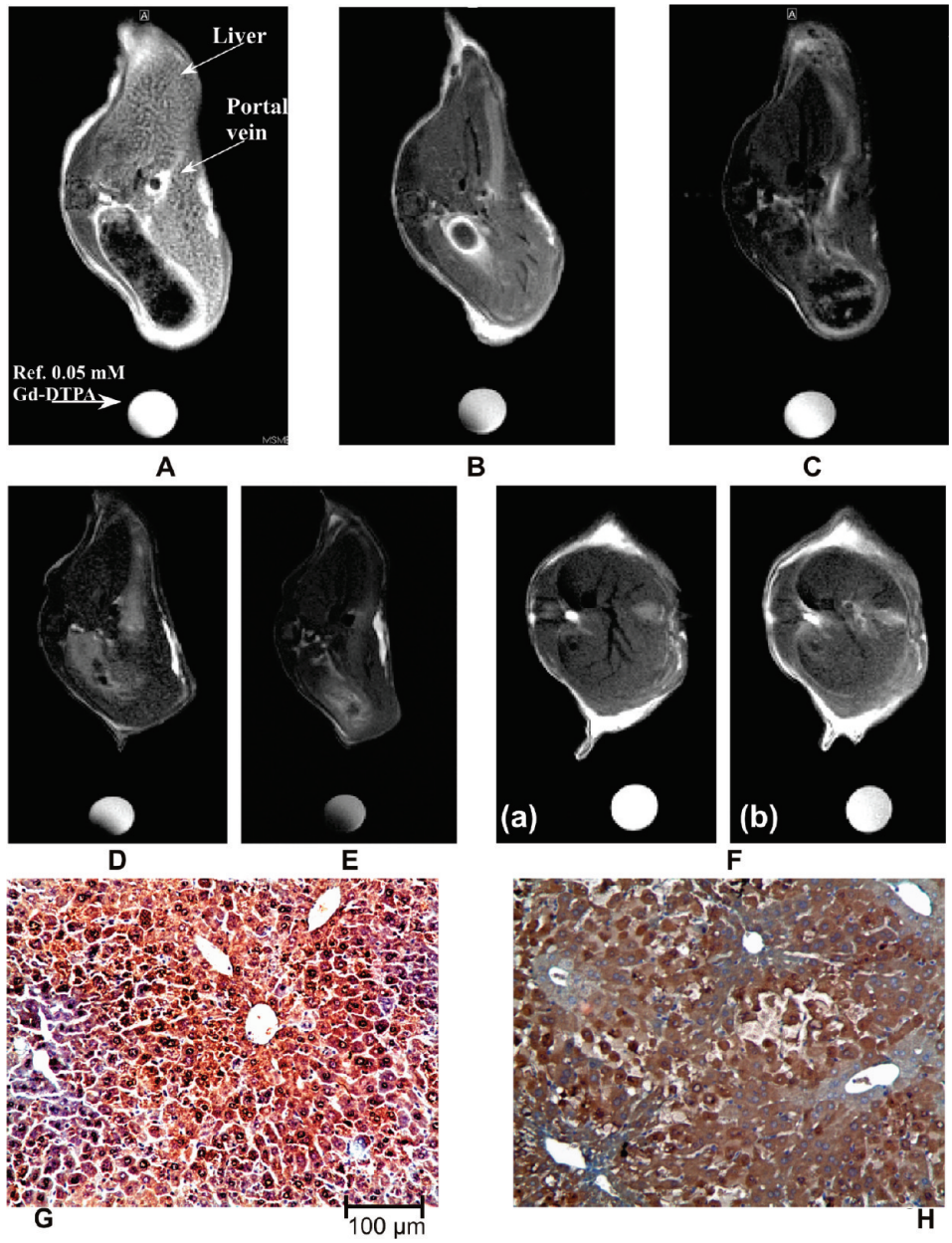

Figure 6. MRI of PS in mouse liver (spatial resolution = 195 μm) 30 min post contrast and immunohistochemistry of apoptotic cells. Apoptotic liver imaged with Gd-DTPA-g-R826 in the absence (A) and in the presence of competitor R826 (B) is compared to healthy liver (C). Apoptotic (D) and healthy (E) liver imaged with Gd-DTPA. (F) Apoptotic liver in precontrast (a) and post injection of Gd-DTPA-g-R826.Sc (b). Apoptotic cells immunostained (brown) with AnnV-Bt (G) and anticaspase-3 antibody (H).

mechanism.[35−37] A major challenge was to understand their activity after membrane binding. A possibility that has emerged was that membrane-associated annexins may function as ion channels and/or as ion channel regulators. Annexins could act thus as both effectors and regulators of ion fluxes and could represent key mediators in the control of cellular Ca^{2+} homeostasis.[35] In the case of peptide R826, its amino acid sequence is homologous with part of the extracellular domain of human transient receptor potential Ca^{2+} channel 5 (L_{358}-*F*-I-K-K-P-F_{364}) and with that of the mouse capacitative Ca^{2+} entry channel 2 (L_{358}-*F*-I-K-K-P-

(35) Gerke, V.; Moss, S. E. Annexins: from structure to function. *Physiol. Rev.* **2002**, *82*, 331–371.

(36) Huber, R.; Berendes, R.; Burger, A.; Schneider, M.; Karshikov, A.; Luecke, H.; Römisch, J.; Paques, E. Crystal and molecular structure of human annexin V after refinement. Implications for structure, membrane binding and ion channel formation of the annexin family of proteins. *J. Mol. Biol.* **1992**, *223*, 683–704.

(37) Kaneko, N.; Ago, H.; Matsuda, R.; Inagaki, E.; Masashi, M. M. Crystal structure of annexin V with its ligand K-201 as a calcium channel activity inhibitor. *J. Mol. Biol.* **1997**, *274*, 16–20.

(38) Okada, T.; Shimizu, S.; Wakamori, M.; Maeda, A.; Kurosaki, T.; Takada, N.; Imoto, K.; Mori, Y. Molecular cloning and functional characterization of a novel receptor-activated TRP Ca^{2+} channel from mouse brain. *J. Biol. Chem.* **1998**, *273*, 10279–10287.

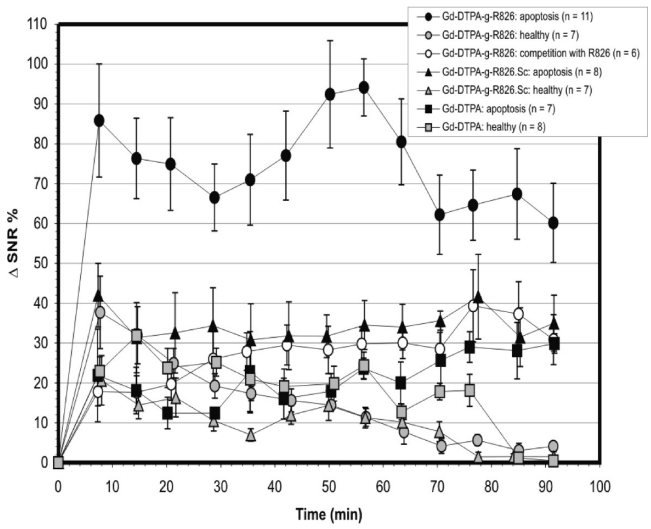

Figure 7. Time evolution of ΔSNR% measured on liver images (means ± SEM).

F_{364}).[38] Interestingly, the human transient receptor potential Ca^{2+} channel 5 is involved in the regulation of membrane PS asymmetry and in the apoptotic signal.[39,40] The alignment of other peptides, identified in the present work, with molecules involved in apoptosis, e.g. Fas antigen ligand or apoptosis associated tyrosine-kinase, is another interesting homology, which proves that peptide selection is not accidental.

According to Montaville et al.,[27] AnnV contains a highly polarized pocket, well adapted to the binding of PS polar head, with a negative (D_{68}, S_{71}, E_{72}) and a positive side (Ca^{2+}, K_{29}, R_{25}, R_{63}). Hence, we have attributed to our amino acids a function in PS (D, E, R, K, H, S, T) and Ca^{2+} (D, E) binding. We may consider that PGDLST and its versions (PGDLSR, PGDLVR, HGDLST) could have the advantage of the balanced distribution of PS and Ca^{2+}-binding sites. We did not perform further tests to confirm the role of Ca^{2+} ions in the interaction with PS, but we may assume that they could have a contribution in the case of PGDLSR and DAHSFS due to the presence of negative charges in their structure.[41] On the other hand, the positive charge conferred by two Lys in the LIKKPF sequence may represent an advantage for the interaction with negatively charged phospholipids. In fact, the two Lys residues resemble the PS binding sites of C_2A domain of synaptotagmin I (Lys_{200} and Lys_{236}).[8] Its estimated hydrophobic property in comparison with the two other peptides may play a role in the interaction with apoptotic cells. Peptide R826 is furthermore relatively stable and its predicted half-life (based on the probability of intracellular ubiquitin mediated degradation) of 5.5 h could be optimal for the time-window of an MRI scanning.

K^*_d values indicated a higher affinity for PS than for PC of PGDLSR and LIKKPF. AnnV itself binds to dioleoyl-PS/dioleoyl-PC bilayers (20% dioleoyl-PS:80% dioleoyl-PC or 100% dioleoyl-PS) with a K_d of $\sim 5 \times 10^{-10}$ M (human AnnV) to 6×10^{-9} M (bovine AnnV) at a 3 mM Ca^{2+} concentration.[25] Although binding of AnnV is stimulated by dioleoyl-PS, its binding is not specific to this phospholipid. Half-maximal binding to cardiolipin, dioleoyl-phosphatidylglycerol, dioleoyl-PS, dioleoyl-PC, phosphatidylinositol, phosphatidic acid, dioleoyl-phosphatidylethanolamine, and sphingomyelin occurs at various Ca^{2+} concentrations, ranging from 0.036 mM (for 100% dioleoyl-PS) to 7 mM (for 20% sphingomyelin/80% dioleoyl-PC).[33]

After peptide synthesis, the ratio IC_{50}/K^*_d highlighted LIKKPF (R826) as the most powerful PS-specific peptide. These results indicate the concentrations of CAs to be used for an efficient targeting by avoiding the interference with endogenous AnnV. For instance, LIKKPF concentration necessary to block the half-maximal binding of AnnV is about 30 times higher than the K_d of AnnV. A paramagnetic CA like Magnevist is injected at a dose of 0.1 mmol/kg. Its blood concentration at T_0 is about 1 mM, which is 106 times higher than the K_d of AnnV.

R826-functionalized CA (Gd-DTPA-g-R826) was assessed first on apoptotic Jurkat cells. These results confirmed the *in vitro* studies presented above, which reflected the efficacy of LIKKPF as a PS-specific binder.

For *in vivo* MRI evaluation, Gd-DTPA-g-R826 was injected into a mouse model of liver apoptosis. Our results suggest that most of the increased liver localization of Gd-DTPA-g-R826 is the consequence of a specific interaction with apoptotic hepatocytes.

Finally, molecular MRI of atherosclerotic plaque was validated on $ApoE^{-/-}$ mice. In postcontrast images it was clearly possible to distinguish anatomical details of the artery wall. Gd-DTPA-g-R826 was not captured nonspecifically by the surrounding tissues, except in the kidneys as a consequence of renal clearance of the CA.

As a PS-specific protein, AnnV was widely used to detect apoptosis in various diseases such as cancer and cardiovascular disorders. For preclinical and clinical studies, AnnV has been radiolabeled with ^{123}I, ^{124}I, ^{125}I, ^{18}F, and ^{99m}Tc for positron emission tomography (PET) and for single-photon emission computed tomography (SPECT) imaging. However, the biodistribution profile of radiolabeled AnnV in humans was found to be not optimal. ^{99m}Tc-imino-AnnV and ^{99m}Tc-(4,5-Bis(Thioacetamido)Pentanoyl)-AnnV (BTAP-AnnV) accumulate in the kidneys, liver, and gut, which makes difficult the imaging of apoptosis in the abdomen with both radiopharmaceuticals. ^{99m}Tc-Hydrazinonicotinamide-AnnV (HYNIC-AnnV) accumulates in kidneys (50% of the injected dose at 3 h after injection) and is taken up by the liver, the red marrow, and the spleen; excretion of the activity was predominantly through the urine (approximately 23% at 24 h). ^{123}I-AnnV accumulates in the stomach and thyroid, and this uptake becomes low in most organs 21 h after administration. The physical half-life of various radioisotopes

(39) Beech, D. J. TRPC1: store-operated channel and more. *Pfluegers Arch.* **2005**, *451*, 53–60.
(40) Abramowitz, J.; Birnbaumer, L. Physiology and pathophysiology of canonical transient receptor potential channels. *FASEB J.* **2009**, *23*, 297–328.
(41) Dragani, B.; Aceto, A. About the role of conserved amino acid residues. *Arch. Biochem. Biophys.* **1999**, *368*, 211–213.

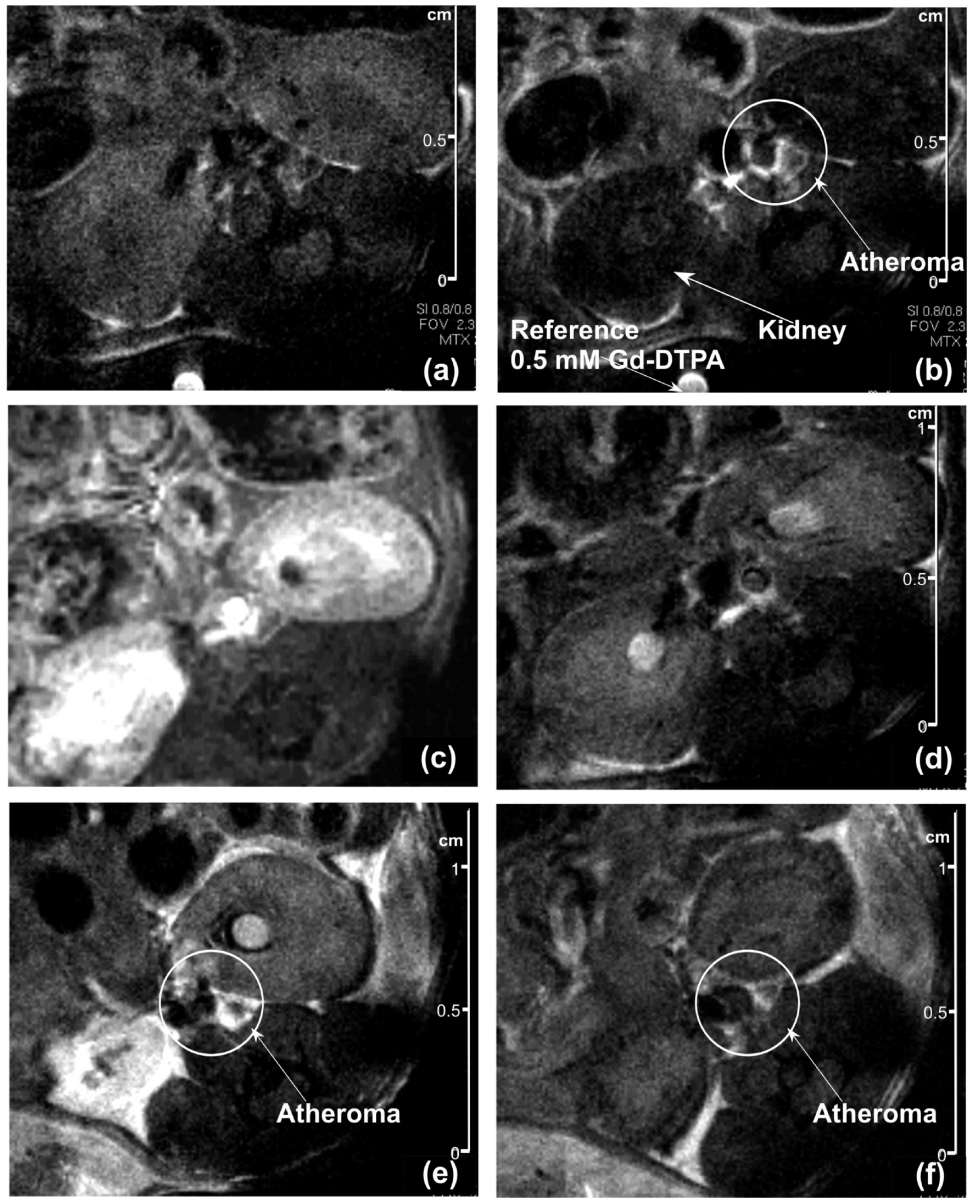

Figure 8. MRI RARE images (spatial resolution = 90 μm) are shown in precontrast (a) and ~30 min post Gd-DTPA-g-R826 (b). They are compared to a TOF image (spatial resolution = 156 × 156 × 625 μm) (c) and to an image obtained post Gd-DTPA (d). The comparison between Gd-DTPA-g-R826 (e) and Gd-DTPA-g-R826.Sc (f) is shown 60 min postcontrast. Images compared in (a)−(d) and those in (e) and (f) are located at the same level of abdominal aorta.

ranges from 6.02 h (for ^{99m}Tc) to 13 h (for ^{123}I) and 60 days (for ^{125}I). Consequently, the choice of the optimum time between the administration of radiolabeled AnnV and the subsequent imaging is a real dilemma because of the coincidence of its biodistribution with the targeted cell death process and because of the limited physical half-life of certain radioisotopes.[42] In addition to this, the ionizing radiation characteristic to radiopharmaceuticals prevents their reiterated administration, inherent to patient monitoring during the treatment program.

Therefore, although AnnV radiolabeled derivatives are widely used for apoptosis detection, these compounds have several limitations. Alternative molecular imaging strategies for cell death detection represent an imperative requirement for the quality of the patient healthcare. As drug candidates, peptides have several advantages over proteins, including their lower manufacturing costs, higher activity per mass, greater stability, lower potential immunogenicity, and better tissue/organ penetration.[14] The peptide-derived CA developed in the present work has thus the advantages of any peptide drug candidate, and is conceived for MRI detection

(42) Boersma, H. H.; Kietselaer, B. L.; J, H.; Stolk, L. M. L.; Bennaghmouch, A.; Hofstra, L.; Narula, J.; Heidendal, G. A. K.; Reutelingsperger, C. P. M. Past, present, and future of annexin A5: from protein discovery to clinical applications. *J. Nucl. Med.* **2005**, *46*, 2035–2050.

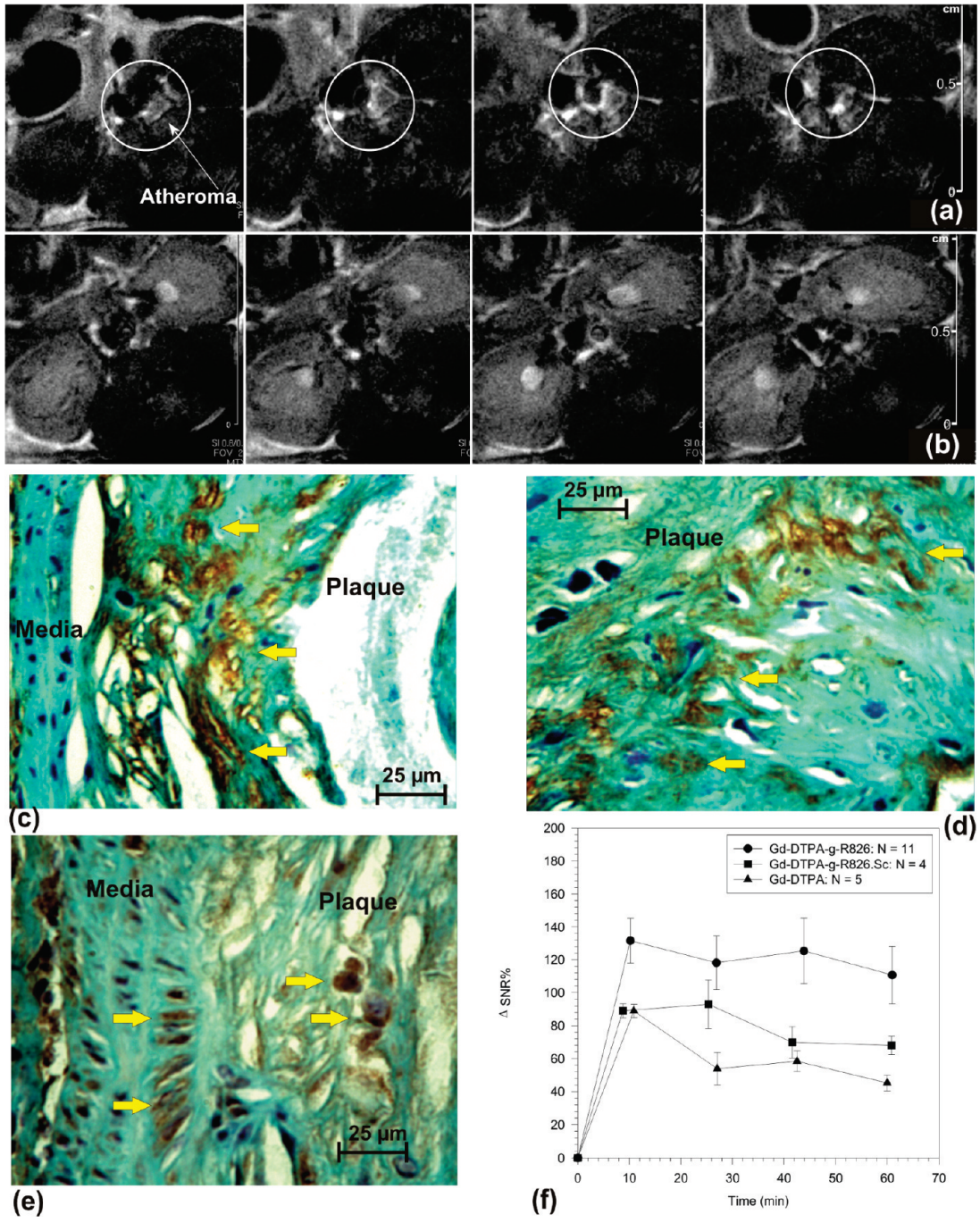

Figure 9. MRI serial slices of abdominal aorta (spatial resolution = 90 μm) 30 min post Gd-DTPA-g-R826 (a) are compared to those obtained post Gd-DTPA (b). Apoptotic cells were immunostained (brown) with AnnV-Bt in the disorganized tunica media (c) and in the plaque head (d) of atherosclerotic aorta; apoptosis was validated with anticaspase-3 antibody (e). Time evolution of ΔSNR% in aorta of ApoE$^{-/-}$ mice is shown in (f).

which is a clinical imaging technique free of any known biological hazard, perfectly suitable for recurrent examination of the patients. This CA did not show a biodistribution significantly different from that of the parent Gd-DTPA complex, as suggested by the MRI studies and by the measurement of gadolinium concentration in organs (data not shown). At about 95 min after administration, the Gd-DTPA-g-R826 concentration in kidneys was 12% ± 4.6% of the injected dose/g (% ID/g) in mice with liver apoptosis and 12% ± 2.2% ID/g in healthy mice. These results were comparable to the biodistribution of Gd-DTPA, which was found in kidneys at a concentration of 14% ± 5.7% ID/g in apoptosis, and of 9% ± 3% ID/g in healthy animals. In spleen, the gadolinium concentration was about 5% ID/g for both compounds in apoptosis, and about 2% ID/g in healthy mice. Gd-DTPA-g-R826 produced a maximum enhancement of apoptotic liver 1 h after administration, while the atherosclerotic plaque was strongly enhanced as early as 11 min after injection. ^{99m}Tc- HYNIC-AnnV produced the same effect at 2 h postinjection both in mice with liver apoptosis[43]

and in atherosclerotic rabbits,[44] probably because of the longer diffusion times required by this large molecule (AnnV has a molecular mass of 36 kDa). In the case of atherosclerotic plaques, the contribution of the blood pool activity attributable to the radiopharmaceutical's characteristic pharmacokinetics could give rise to artifacts that may be misinterpreted as plaque uptake. This is not the case with MRI, which has intrinsic technological strategies for the saturation of blood signal. MRI offers in addition a perfect anatomical resolution which is adapted for the in-depth inspection of the vascular wall territory. To our knowledge, no Gd-labeled AnnV derivative was described to date for MRI applications, probably due to the cost of large protein quantities required for such investigations.

The inherent low sensitivity of low molecular weight paramagnetic imaging probes, as the Gd-DTPA-g-R826, may represent the major limitation of apoptosis detection by MRI in areas characterized by low PS concentration. Owing to their large NMR efficacy (i.e., relaxivity), iron oxide nanoparticles may represent an attractive probe alternative[45] after their functionalization with the PS-targeted peptide.

Our PS-targeted peptide identified by phage display could thus have a real potential in the diagnosis of atherosclerotic disease and of other apoptosis-associated pathologies, such as cancer, ischemia, chronic inflammation, autoimmune disorders, transplant rejection,[6] neurodegenerative disorders,[46] and diabetes mellitus.[47] In the case of cardiovascular diseases, apoptosis has various implications and is associated with loss of cardiomyocytes subsequent to myocardial infarction, atherosclerotic plaque instability, congestive heart failure and allograft rejection of the transplanted heart.[15]

There is growing evidence that apoptosis contributes to the instability of atherosclerotic lesion. Although the consequences of cell death within the advanced lesion are not precisely defined, morphological data suggest that macrophage apoptosis contributes substantially to the size of the necrotic core,[6] whereas apoptosis of SMC results in thinning of the fibrous cap.[48] It has also been proposed that extensive macrophage apoptosis occurs at sites of plaque rupture and possibly contributes to this process.[49] Consequently, apoptosis detection may help to identify lesions prone to rupture and several scintigraphic imaging agents have been developed by various groups based on AnnV, which is captured by plaques containing markers of instability, including macrophages, infiltrates and intraplaque hemorrhage.[49]

Acknowledgment. The authors thank Mrs. Patricia de Francisco for her help in preparing the manuscript, and Prof. Gérard Toubeau and Mrs. Annik Maes for their technical assistance in immunohistochemistry studies.

MP900106M

(43) Blankenberg, F. G.; Katsikis, P. D.; Tait, J. F.; Davis, R. E.; Naumovski, L.; Ohtsuki, K.; Kopiwoda, S.; Abrams, M. J.; Darkes, M.; Robbins, R. C.; Maecker, H. T.; Strauss, H. W. In vivo detection and imaging of phosphatidylserine expression during programmed cell death. *Proc. Natl. Acad. Sci. U.S.A.* **1998**, *95*, 6349–6354.

(44) Kolodgie, F. D.; Petrov, A.; Virmani, R.; Narula, N.; Verjans, J. W.; Weber, D. K.; Hartung, D.; Steinmetz, N.; Vanderheyden, J. L.; Vannan, M. A.; Gold, H. K.; Reutelingsperger, C. P.; Hofstra, L.; Narula, J. Targeting of apoptotic macrophages and experimental atheroma with radiolabeled annexin V: a technique with potential for noninvasive imaging of vulnerable plaque. *Circulation* **2003**, *108*, 3134–3139.

(45) Laurent, S.; Forge, D.; Port, M.; Roch, A.; Robic, C.; Vander Elst, L.; Muller, R. N. Magnetic iron oxide nanoparticles: synthesis, stabilization, vectorization, physicochemical characterizations, and biological applications. *Chem. Rev.* **2008**, *108*, 2064–2110.

(46) Tatton, W. G.; Chalmers-Redman, R. M.; Ju, W. Y.; Wadia, J.; Tatton, N. A. Apoptosis in neurodegenerative disorders: potential for therapy by modifying gene transcription. *J. Neural. Transm. Suppl.* **1997**, *49*, 245–268.

(47) Cnop, M.; Welsh, N.; Jonas, J. C.; Jörns, A.; Lenzen, S.; Eizirik, D. L. Mechanisms of pancreatic β-cell death in type 1 and type 2 diabetes many differences - few similarities. *Diabetes* **2005**, *54*, S97–S107.

(48) Geng, Y. J.; Henderson, L. E.; Levesque, E. B.; Muszynski, M.; Libby, P. Fas is expressed in human atherosclerotic intima and promotes apoptosis of cytokine-primed human vascular smooth muscle cells. *Arterioscler. Thromb. Vasc. Biol.* **1997**, *17*, 2200–2208.

(49) Kietselaer, B. L.; Reutelingsperger, C. P.; Heidendal, G. A.; Daemen, M. J.; Mess, W. H.; Hofstra, L.; Narula, J. Noninvasive detection of plaque instability with use of radiolabeled annexin A5 in patients with carotid-artery atherosclerosis. *N. Engl. J. Med.* **2004**, *350*, 1472–1473.